Cryo-EM structure of lipid embedded human ABCA7 at 3.6Å resolution

Le Thi My Le[1]†, James R. Thompson[1]†, Tomonori Aikawa[2], Takahisa Kanikeyo[2] & Amer Alam[1,*]

[1]The Hormel Institute, University of Minnesota, Austin, Minnesota 59912

[2]Department of Neuroscience, Mayo Clinic, Jacksonville, Florida 32224

†These authors contributed equally to this work

*Address correspondence to: Amer Alam, PhD, aalam@umn.edu

Abstract

Dysfunction of the ATP Binding Cassette (ABC) transporter ABCA7 alters cellular lipid homeostasis and is linked to Alzheimer's Disease (AD) pathogenesis through poorly understood mechanisms. Here we determined the cryo-electron microscopy (cryo-EM) structure of human ABCA7 in a lipid environment at 3.6Å resolution that reveals an open conformation, despite bound nucleotides, and bilayer lipids traversing the transmembrane domain (TMD). We show that ATP hydrolysis in ABCA7 is modulated by its lipid environment as well as apolipoprotein (apo) A1 and apoE, the latter in an isoform dependent manner, and that apoA1 can directly bind ABCA7. Structural similarities between ABCA and ABCG family transporters suggest that TMD-nucleotide binding domain (NBD) pairs in both sets move as single rigid bodies to affect conformational transitions. Our data suggest these transitions in ABCA7 are influenced by TMD cavity lipids and apolipoprotein binding in addition to being coupled to ATP hydrolysis.

46 **Introduction**

47 AD accounts for the overwhelming majority of dementias, affecting more than 5.5 million people
48 in the United States alone. In the absence of a cure, this number is expected to increase rapidly,
49 with devastating healthcare and socioeconomic consequences (Alzheimer's Association, 2020).
50 Genome wide association studies have identified *ABCA7* as an important genetic risk factor for
51 AD. ABCA7 single nucleotide polymorphisms and coding variants are linked to AD pathogenesis
52 through dysregulated or diminished transporter function (Almeida et al., 2018; Bellenguez et al.,
53 2017; De Roeck et al., 2019; Hollingworth et al., 2011; Lambert et al., 2013; Le Guennec et al.,
54 2016; Ma et al., 2018; Swerdlow, 2016). Targeting ABCA7 may therefore offer a new way forward
55 to facilitate development of novel AD therapeutics. To this end, understanding the molecular
56 details of ABCA7 lipid interactions, its substrate transport cycle and its regulation, and the
57 physiological consequences of ABCA7 dysfunction is a fundamental prerequisite for realization
58 of ABCA7 directed AD therapeutic regimens.

59 ABCA7 encodes a 2146 amino acid membrane transporter that is expressed in low abundance in
60 many tissues and blood (Iwamoto et al., 2006; Sleegers, 2020). It bears similarities to the
61 phospholipid and sterol transporter ABCA1, with which it shares ~54% sequence similarity and
62 functional overlap, as well as the retinal importer ABCA4. The latter is functionally distinct from
63 ABCA7 and ABCA1 with an opposite direction of substrate transport. All three are expressed as
64 single polypeptides comprising two non-identical halves. Each half consists of a TMD, with the
65 first two transmembrane helices (TMs) of each separated by a large extracellular domain (ECD),
66 and an NBD attached to a cytoplasmic regulatory domain (RD) of largely unknown function (Qian
67 et al., 2017). ABCA7 and ABCA1 are distinguished from each other by several functional
68 differences. First, they have reportedly different phospholipid specificities (Quazi and Molday,

69 2013; Tomioka et al., 2017). Second, while the role of ABCA1 in the formation of high-density
70 lipoprotein (HDL) particles is firmly established, HDL formation by ABCA7 has only been shown
71 in transiently transfected cells and the resulting HDL particles are reportedly smaller than those
72 produced by ABCA1 with a reduced cholesterol content. While ABCA7 therefore serves as a
73 useful model for studying ABCA transporter and apolipoprotein interactions, its physiological role
74 in cellular HDL generation is as of yet unclear. Third, ABCA7 and ABCA1 expression are
75 inversely regulated by cellular cholesterol, with the former downregulated by cholesterol
76 accumulation and the latter upregulated (Ikeda et al., 2003; Iwamoto et al., 2006). Moreover, only
77 ABCA1 dysfunction has been conclusively linked to hypercholesterolemia and atherosclerosis
78 (Meurs et al., 2012; Voloshyna and Reiss, 2011). Finally, both transporters share sequence
79 similarities with the *C. elegans* cell corpse engulfment protein (ced-7: 24% identical to ABCA7),
80 which regulates phagocytosis during programmed cell death (Wu and Horvitz, 1998). However,
81 only depletion or dysfunction of ABCA7 impairs phagocytosis, which is linked to AD through a
82 role in amyloid beta and tau plaque clearance, in mouse fibroblasts, macrophages, and microglia
83 (Abe-Dohmae, 2012; Tanaka et al., 2010).

84 While the structures of detergent purified ABCA1 and ABCA4 in a nucleotide free and ATP bound
85 conformation have been determined (Liu et al., 2021; Qian et al., 2017), no ABCA7 structure is
86 currently available. The TMD conformation in both nucleotide free structures showed a
87 transmembrane cavity open to the outside with extraneous density purportedly from ordered
88 phospholipids or detergent molecules seen close to the cytoplasmic gate. While these structures
89 have greatly advanced our understanding of the overall architecture of ABCA family transporters,
90 the key question of what the TMDs looks like in a lipid environment remains open. Moreover,
91 there is currently no consensus on how apolipoproteins affect conformational changes, if any, to

92 influence the lipid transfer activity of ABCA7 and ABCA1. To shed light on these mechanistic
93 aspects of ABCA7 functioning, we purified human ABCA7 from human embryonic kidney (HEK)
94 cells, reconstituted it in phospholipid nanodiscs, and carried out its structural and functional
95 characterization. Our results allow us to begin addressing the influence of lipids and
96 apolipoproteins on ABCA7, providing a general mechanistic framework applicable to other ABCA
97 family transporters, many of whose functions remain understudied at the molecular level. These
98 results open the door for new directions for investigating a functional link between ABCA7 and
99 apoE isoforms and will be of significant interest to medicinal chemists and computational
100 biologists targeting ABCA7 for *in silico* studies.

101 **Results**

102 **Phospholipids and apolipoproteins modulate ABCA7 *in vitro* activity**

103 We expressed human ABCA7 harboring a C-terminal yellow fluorescent protein (YFP)-rho-ID4
104 tag in a tetracycline inducible stable HEK293 cell line. This system has reproducibly yielded high
105 quality preparations of functional ABC transporters devoid of contaminating phosphatases (Alam
106 et al., 2018; Nosol et al., 2020; Olsen et al., 2020). Purified ABCA7 was reconstituted in
107 phospholipid nanodiscs and its ATP hydrolysis activity was analyzed (Figure 1A-C, Figure S1A-
108 B). The nanodisc platform provides a more physiological *in vitro* system for studying integral
109 membrane proteins including other ABC transporters in multiple conformations and allowed us to
110 mimic the expected native membrane bilayer environment of ABCA7 and control its lipid and
111 cholesterol composition. As seen in Figure 1A, nanodsic reconstituted ABCA7 displayed a basal
112 ATPase rate of ~30 nmol min^{-1} mg^{-1} in nanodiscs comprising a mixture of Brain Polar Lipids and
113 Cholesterol (BPL/Ch). ATPase rates were highest in nanodiscs enriched in brain polar

114 phosphatidylethanolamine (PE), followed by phosphatidylserine (PS) and phosphatidylcholine
115 (PC). Removal of cholesterol led to an increase in ATPase rate, in agreement with previous
116 analyses of liposome reconstituted ABCA7 (Quazi and Molday, 2013). ATP hydrolysis in
117 nanodiscs, liposomes, and detergents followed Michaelis-Menten reaction kinetics with Michaelis
118 constant (K_M) values of 0.4 mM, 0.8mM and 0.8 mM, respectively (Figure 1B). ATPase activity
119 was inhibited by both sodium orthovanadate and the non-hydrolysable ATP analog ATP gamma
120 S (γS) and stimulated by 2,4-diamino-6,7-dimethoxyquinazoline (DADMQ), a metabolite
121 identified from a metabolomics screen comparing wildtype and ABCA7 heterozygous knockout
122 mice (Figure S1B) (unpublished data). This suggests modulation of ABCA7 activity by not only
123 lipids and sterols, but also select small molecules, and the possibility of DADMQ being an ABCA7
124 agonist.

125 Cells expressing ABCA7 have been shown to directly bind apoA1 (Wang et al., 2003), although
126 the exact nature of these interactions is poorly understood. We compared the ATPase activity of
127 detergent purified ABCA7 in the presence of a molar excess of human apoA1, apoE2, apoE3 or
128 apoE4. As shown in Figure 1C, all four recombinant apolipoproteins stimulated ATPase activity
129 above that of detergent solubilized ABCA7 alone. This suggests a direct interaction between the
130 apolipoproteins and ABCA7 that leads to conformational changes resulting in a rearrangement of
131 the NBDs to facilitate ATP hydrolysis. This ATPase rate stimulation is reduced for the E2 variant
132 and almost abolished for the E4 variant, suggesting an altered binding interaction between the
133 apoE isoforms and ABCA7. It is interesting to note that while the apoE4 variant is correlated with
134 increased AD risk and the E2 variant is considered protective, both appear to have a weaker
135 interaction with ABCA7 based on ATPase stimulation. To confirm a direct interaction between
136 ABCA7 and apolipoproteins, we immobilized his-tagged apoA1 on Nickel- nitrilotriacetic acid

137 (Ni-NTA) resin in the presence of detergent solubilized ABCA7. As seen in Figure 1D, ABCA7
138 is retained and subsequently co-elutes with apoA1, providing qualitative confirmation of direct
139 complex formation that we speculate holds true for apoE isoforms as well.

140 **Cryo-EM structure of ABCA7 reveals lipid filled TMD cavity**

141 The cryo-EM structure of nanodisc reconstituted ABCA7 was determined to 3.6Å resolution in
142 the presence of ATPγS (Figure 1E, Figure S1C-E). Despite the addition of nucleotide, ABCA7
143 was seen to adopt an open conformation with separated NBDs similar to that seen for apo human
144 ABCA1 and ABCA4, which we speculate arises from interactions between TMD2 and the ECD
145 as explained below. However, unlike the ABCA1 and ABCA4 structures, the central cavity
146 between TMD1 and TMD2 of ABCA7 reveals density features consistent with a single file of
147 bilayer phospholipids traversing the width of the TMDs (Figure 1F). While we cannot ascertain
148 the lipid identities, their specific orientation, nor exclude the presence of other sterols or lipidic
149 species, likely due to the mobile nature of the observed membrane patch that leads to transient
150 occupancies, these density features are distinguishable from the more delocalized and
151 discontinuous density of the surrounding nanodisc lipids and characterized by 1) a gap between
152 the upper and lower leaflet density features and 2) a gap between the two acyl chains of a single
153 file of phospholipids in both leaflets (Figure 1F, Figure 2A-B). The phospholipids appear
154 continuous with the surrounding membrane except at the intracellular gate formed by residues
155 L655 and T1646 from TM5 and TM11, respectively (Figure 2B). TM1, TM2, and TM5 from
156 TMD1 contribute the majority of residues within 5 Å of the observed phospholipids compared to
157 only TM11 from TMD2 (Figure 2C). This asymmetric arrangement with a smaller TMD2 interface

158 arises from a rigid body shift of the TMD2-NBD2 pair of ABCA7 compared to the more symmetric
159 arrangement seen in the ABCA1 structure, as expanded upon below.

160 **Details of TMD-ECD and lipid facing interfaces of ABCA7**

161 What leads to the observed asymmetry in TMD arrangement in ABCA7 compared to apo ABCA1
162 and ABCA4? As seen in Figure 3, the electrostatic potential maps of cavity facing interfaces in
163 ABCA7 reveal marked differences between the two TMDs. The TMD1 interface is significantly
164 more electropositive than that of TMD2 (Figure 3A-B), particularly along the cytoplasmic and
165 extracellular boundaries where cavity facing residues are likely to be in close proximity to any
166 TMD resident lipids. In contrast, the less electropositive TMD2 interface comprises a series of
167 negative charges on its extracellular boundary. This may serve to repel phospholipid headgroups
168 and could account for the increased conformational mobility of TMD2 in the presence of TMD
169 phospholipids. In addition to TMD1, the base region of the ECD comprises a cluster of positively
170 charged residues (Figure 3C), continuous with TMD1. An analysis of the TMD-ECD interfaces
171 (Figure 3D) reveals much more extensive contacts between the ECD and TMD1 (buried surface
172 area of ~790 $Å^2$) compared to TMD2 (~330 $Å^2$ buried surface area). Both TMD1 and TMD2 make
173 contacts with the opposite ECD subunits, leading to a domain swapped arrangement that may be
174 important for coupling interdomain conformational changes. The TMD1-ECD2 interface (~565
175 $Å^2$) is significantly larger than that of TMD1-ECD1 (~223 $Å^2$) and both interfaces comprise an
176 extensive network of polar and electrostatic interactions. Positively charged residues from the ECD
177 located above the TMD cavity are oriented towards the upper leaflet, part of a cluster of positive
178 charges from ECD1, ECD2, and TMD1 that could promote passage of phospholipids to the ECD
179 from the TMD.

180 Our ABCA7 structure allows us to map known missense ABCA7 variants and also
181 compare known ABCA1 missense variants to analyze conservation in ABCA7. As shown in
182 Figure 4, many pathogenic missense ABCA7 mutants associated with higher AD risk, as well as
183 three 'protective' missense variants reported to reduce AD risk are found distributed over the entire
184 ABCA7 structure. Many of these overlap with residues comprising the TMD-ECD interfaces.
185 Within the ECD, three neighboring residues map locations of homologous ABCA1 missense
186 mutants associated with Tangier's Disease that all reduce ABCA1 interaction with apoA1 as
187 measured using cross-linking ability with both phospholipid- and water-soluble agents (Fitzgerald
188 et al., 2002). Due to the structural homology between ABCA7 and ABCA1, we believe these
189 residues loosely demarcate a putative interface that both transporter proteins use when interacting
190 with apolipoproteins in order to initiate phospholipid efflux from cells to create HDL. In fact,
191 several known pathogenic mutations in ABCA1 that may have a similar effect in ABCA7, based
192 on conservation of the associated residues, are clustered in this region of the ECD above the TMD
193 cavity. On the cytoplasmic side of the transporter, of particular interest is the VFVNFA motif in
194 ABCA1 (Fitzgerald et al., 2004) that has been shown to be essential for phospholipid efflux and
195 apoA1 binding. The equivalently placed VFLYFS motif in ABCA7, while not identical, may play
196 a similar role, suggesting a possible conserved role for the ABCA family RDs in coupling long
197 range conformational changes with the ECD as discussed below. Finally, EM density likely
198 arising from bound phospholipids or cholesterol was also observed in the hydrophobic tunnel
199 within the ECD (Figure 3E), similar to observations from the structure of ABCA1 (Qian et al.,
200 2017). The tunnel has two possible portals that are solvent accessible and was previously suggested
201 to be a temporary space to sequester phospholipids in ABCA1 or serve as a passage for
202 phospholipid transport to apolipoproteins, a postulate supported by our observations in ABCA7.

203 The observed ECD lipids are predominantly located within ECD1, which contributes the majority
204 of residues within 5Å of them.

205 **Conserved rigid body motions define ABCA7 conformational transitions**

206 Differences in local EM density quality in our ABCA7 maps (Figure S2) suggest increased motion
207 in TMD2 and NBD2, while TMD1-NBD1 and the ECD appear to be more rigid. This is further
208 evidenced by a comparison of our ABCA7 structure with that of ABCA1. As shown in the
209 superposition in Figure 5A, TMD1-NBD1 and the ECD base region display a high degree of
210 structural similarity. However, the TMD2-NBD2 pair undergoes a rigid body shift, involving an
211 outward translation and rotation to a wider open conformation. This leads to an opening of the
212 intracellular gate, marked by the increase in C alpha distances between the two intracellular gate
213 forming residues L655 and T1646 (Figure 4B-C). Interestingly, this shift is also accompanied by
214 a rigid body movement of the entire regulatory domain (RD), which moves as a single unit despite
215 comprising two halves sequentially far apart (Figure 4D). Whereas the RD of ABCA1 maintains
216 molecular interactions with both NBD1 and NBD2, the ABCA7 RD separates from NBD2 while
217 maintaining contact with NBD1. Despite the overall structural change affected by these
218 conformational transitions, individual TMD-NBD pairs and RD share virtually identical
219 architectures, further highlighting that rigid body movements involved (Figure S4).

220 To establish whether the rigid body motions outlined above extend to other ABC transporters of
221 the Type-V fold (Thomas et al., 2020), we extended our analysis of individual TMD-NBD pairs
222 to members of the G family for which structural data is available, namely ABCG2 and ABCG5/G8
223 (Figure 6A). As shown in Figure 6B, TMD-NBD pairs from both the apo open (Orlando and Liao,
224 2020) and ATP bound closed conformation of ABCG2 (Manolaridis et al., 2018) share a virtually

225 indistinguishable conformation (Figure 6B, left), also shared by ABCG5 and ABCG8 (Lee et al.,
226 2016) (Figure 6B, center). ABCG and ABCA members share mirrored topologies with the former
227 arranged in an NBD-TMD configuration compared to TMD-NBD for the latter. However, the
228 individual TMD-NBD pairs from ABCA7 share strong structural similarities with those of ABCG2
229 (Figure 6B, right). This suggests the possibility of ABCA family transporters undergoing the same
230 conformational transitions seen in the ABCG family (Figure 6C). The physiological implications
231 of this are expanded upon below.

232 **Discussion**

233 Our data address several unknowns about the physiological functioning of ABCA7. First, we show
234 that the large TMD cavity seen in the open conformation of ABCA7 is completely lipid filled. The
235 uninterrupted passage of phospholipids from the upper leaflet of the surrounding membrane
236 through the ABCA7 TMD raises the possibility that phospholipid efflux, and therefore ABCA7's
237 role in phospholipid homeostasis, may vary by cell type and be influenced by inherent asymmetry
238 in phospholipid distribution between the two bilayer leaflets. By breaking the bilayer's
239 cytoplasmic phospholipid leaflet, TM5 and TM11 may facilitate the extrusion of phospholipids
240 from the upper leaflet of ABCA7. Positively charged cavity facing interfaces of TMD1 and its
241 ECD interface may aid lipid accessibility to the cavity and, subsequently, to the ECD base region
242 for sequestration in the hydrophobic ECD tunnel.

243 Second, our comparison of ABCA and ABCG family transporters shows that transporters
244 in these families may share common TMD-NBD cores that move in tandem as rigid bodies to
245 affect overall conformational changes. This is unlike type-IV exporters such as members of the
246 ABCB and ABCC families that 1) have a domain swapped architecture and 2) undergo
247 rearrangements of individual TMs and TM pairs during the transport cycle (Lee et al., 2014). This

248 leads us to propose that the ABCA7 TMD-NBD pairs of ABCA7 may follow a similar set of
249 movements associated with nucleotide dependent NBD dimerization and suggest the possibility of
250 an ABCA7 conformation similar to that seen in the ATP bound $ABCG2_{EQ}$ structure. The transition
251 to a closed ABCA7 structure would therefore only entail rigid body movements of the two halves
252 of the protein barring steric hindrance from the ECD or RD (Figure 6C).

253 Based on the smaller ECD and RD interfaces involved, we postulate that the TMD2-NBD2
254 pair is the mobile rigid body unit involved in open to closed transitions in ABCA7. This would
255 entail some form of interfacial disengagement of the ECD from one or both of the TMDs, allowing
256 the TMDs to approach each other in the closed state similar to those of ABCG2. One possible way
257 this could be accomplished would be the binding of apolipoproteins that may cause conformational
258 changes promoting NBD closure. This is further supported by the observation that the hydrolysis
259 deficient EQ mutant of ABCA4 adopts a closed conformation with bound ATP that is accompanied
260 by a reconfiguration of the ECD and TMD2 interface. We show that the ATPase activity of
261 ABCA7 is enhanced in the presence of apolipoproteins, suggesting a direct interaction that may
262 contribute to structural changes in the ECD that are coupled to NBD arrangement. This is in line
263 with data suggesting apoA1 mediated structural changes in ABCA1 (Nagao et al., 2012) and
264 further evidenced by the fact that despite the clear indication of bound nucleotides, we were unable
265 to resolve 3D classes with dimerized NBDs in our EM datasets, which would require
266 rearrangements of the TMD-ECD interface.

267 Inter-domain rigidity appears to play a key role in relaying long range conformational
268 changes in ABCA7. Individual TMD-NBD pairs move in concert to control access to a central
269 phospholipid cavity. ECD1 and ECD2 both maintain contacts with the opposing TMDs, adding an

270 element of domain swapping that could play a role in coupling the two halves of the protein.
271 Similarly, while the RD appears to move as one rigid unit, RD1 makes contacts with both NBDs,
272 possibly further contributing to both halves of the transporter being conformationally coupled. The
273 VFLYFS motif in RD2 (equivalent to VFVNFA in ABCA1) shown to affect phospholipid
274 translocation may aid in stabilizing the TMD2-NBD2 pair. In line with this, the RD configuration
275 seen in ABCA1 and ABCA4 structures adopts more symmetric contacts with the two NBDs, with
276 the two halves of ABCA1 and ABCA4 consequently appearing more homogenous in terms of their
277 local structure. While the intracellular gate in our ABCA7 structure adopts a more open
278 conformation compared to ABCA1 and ABCA4, the difference may be a consequence of the
279 absence of phospholipids in the latter two.

280 Taken together, our data allow us to put forward a hypothetical model for how
281 apolipoprotein-mediated structural changes in ABCA7 and, by extension, ABCA1, may occur
282 (Figure 6D). In the absence of apolipoproteins, ABCA7 adopts an open configuration with a large,
283 central lipid filled cavity open to both bilayer leaflets. The TMD-ECD interfaces in this state afford
284 enough flexibility to allow for a TMD configuration similar to that seen in the open conformation
285 of detergent purified ABCA1 and ABCA4 (dashed lines in figure 6D). The binding of
286 apolipoproteins to ABCA7 may rearrange the ECD and its TMD interactions in a way that
287 promotes TMD2-NBD2 to collapse into TMD1-NBD1 in a closed state (red arrows in figure 6D).
288 This would necessitate the exit of any TMD cavity resident lipids that could occur by the extraction
289 of a subset towards the ECD and/or laterally back into the surrounding lipid environment.
290 Apolipoprotein bound ABCA7 could then cycle back and forth between open and closed states in
291 an ATPase hydrolysis dependent manner, repeating the cycle of lipid entry and exit from TMDs
292 in the process. Disengagement of apolipoproteins, possibly in a lipid filled state, would then shift

293 the conformational equilibrium back to favoring the open state (black arrows in Figure 6D). Given
294 our model, the reduced ATPase stimulation observed for apoE4 compared to apoE3 points to a
295 weaker interaction between apoE4 and ABCA7. Our data therefore offer a direct link between
296 two of the highest genetic risk factors for AD progression, *APOE4* and *ABCA7*, and open up the
297 possibilities for future studies analyzing this direct interaction in context of AD patients carrying
298 mutations in one or both.

299 Despite significant progress in our understanding of ABCA family transporter structure,
300 several questions about the mechanistic details of their physiological functioning remain open,
301 with several new ones emerging. First, it is yet unclear if ABCA7 and ABCA1 lipid flipping and
302 export properties are connected (Quazi and Molday, 2013; Tomioka et al., 2017). Elucidation of
303 the exact mechanisms involved will shed light on the possible role ABCA7 may play in lipid
304 asymmetry and whether reduced ABCA7 function leads to alterations that may influence cellular
305 phagocytic response. Second, while our data suggests apoE influences ABCA7 activity in an
306 isoform dependent manner, the physiological consequences of this, primarily the reduced effect of
307 the AD related apoE4 mutant, require further study, especially in light of data showing no isoform
308 dependent differences in apoE mediated efflux of lipids in ABCA7 expressing cells (Tomioka et
309 al., 2017). Finally, the underlying molecular basis for lipid specificity in ABCA7 is as of yet poorly
310 understood and requires detailed structural analysis in distinct lipid environments.

311 **METHODS**

312 **ABCA7 expression and purification**

313 We utilized the Flp-In TREX system (Thermo Fisher Scientific) for tetracycline inducible
314 expression of human ABCA7. In short, a codon optimized synthetic gene construct
315 (Geneart/Thermo Fisher Scientific) of isoform 1 of ABCA7 (Uniprot ID Q8IZY2-1) harboring a

316 C-terminal eYFP-Rho1D4 tag (Molday and Molday, 2014) with a 3C/precision protease site
317 between the protein and purification tags was cloned into a PCDNA5.1 FRT/TO vector between
318 BamHI and NotI restriction sites and a stable cell line was generated as per manufacturer's
319 protocol. The resulting HEK293 based stable cells were grown and maintained in adherent cell
320 culture in Dulbecco's Modified Eagle Medium (DMEM, Thermo Fisher Scientific) supplemented
321 with 10% Fetal Bovine Serum and a penicillin / streptomycin mixture (Thermo Fisher Scientific)
322 at 37°C with 5% carbon dioxide (CO_2) under humidified conditions. For protein production, cells
323 were induced with 0.6 ug ml^{-1} tetracycline at a confluency of ~80% in fresh DMEM supplemented
324 with 2% FBS under otherwise identical conditions for an additional 72 hours before being washed
325 with Phosphate Buffered Saline, harvested, and flash frozen in liquid nitrogen.

326 For purification, thawed cells were resuspended in a lysis buffer (Buffer L) comprising 25 mM
327 Hepes pH 7.5, 150 mM sodium chloride (NaCl), 20% glycerol, and a protease inhibitor cocktail
328 containing 1 cOmplete EDTA free inhibitor tablet (Roche) per 50ml Buffer L, 800 μM
329 phenylmethylsulfonyl fluoride (PMSF), and 10 μg ml^{-1} soybean trypsin inhibitor (both Sigma),
330 and mechanically cracked using a dounce homogenizer before addition of a 0.5%/0.1% w:v
331 mixture of Dodecyl maltoside (DDM) and Cholesteryl hemisuccinate (CHS) (both Anatrace).
332 Protein extraction was allowed to proceed for 90 minutes at 4°C with gentle agitation after which
333 the suspension was centrifuged at 40,000 rcf for 30 minutes and the supernatant applied to rho-
334 1D4 antibody (University of British Columbia) coupled to cyanogen bromide activated sepharose
335 resin (Cytiva). Binding was allowed to proceed for 3 hours before the unbound fraction was
336 discarded and beads washed with 4 x 10 bed volumes (BVs) of wash buffer (25 mM Hepes pH
337 7.5, 150 mM NaCl, 0.02%/0.004 % w:v DDM/CHS). Protein was eluted by incubation with 3 BVs

338 elution buffer (wash buffer supplemented with either 3C protease (1:10 w:w 3C:ABCA7) or 0.5
339 mg ml^{-1} 1D4 peptide (genscript)) for 2-18 hours.

340 **apoA1 production and pull-down assay**

341 A synthetic construct of apoA1 bearing a 3C protease cleavable N-terminal decahistidine tag
342 (Geneart/Thermo Fisher Scientific) was cloned into a pET28a vector (addgene) and transformed
343 in *E. coli* BL21 DE3 cells (New England Biolabs). One-liter cultures of Terrific Broth (TB)
344 supplemented with 50 ug ml^{-1} kanamycin were grown from 10 ml overnight cultures from single
345 colonies grown in LB. Cells were grown to an OD600 of 0.8 in a shaking incubator at 37 °C and
346 induced with 1 mM isopropyl β-d-1-thiogalactopyranoside (IPTG). Protein expression was
347 allowed to proceed at 20°C for 12 hours. Cells were centrifuged at 12,000 rcf, and pellets were
348 flash frozen in liquid nitrogen and stored at -80°C until required. Frozen pellets were resuspended
349 in 8 ml/ gram cell pellet resuspension buffer comprising 25 mM Hepes pH 7.5, 150 mM NaCl and
350 1 mM phenylmethylsulfonyl fluoride (PMSF) and sonicated. The suspension was spun down at
351 16,000 rcf at 4 °C for 30 min and the supernatant was applied 5 ml Ni-NTA resin (Qiagen) / L
352 culture medium. After discarding the flowthrough, the resin was washed with 25 mM Hepes pH
353 7.5, 150 mM NaCl, 1 mM PMSF and 20 mM imidazole until a pre-established baseline A280
354 reading was achieved. ApoA1 was eluted in 4 BVs of 25 mM Hepes pH 7.5, 150 mM NaCl, 1 mM
355 PMSF and 200 mM imidazole, concentrated using a 10 kDa molecular weight cutoff (MWCO)
356 amicon filter (Millipore-Sigma) and desalted using a PD10 column (cytiva) into 25 mM Hepes pH
357 7.5, 150 mM NaCl. The concentration of apoA1 was adjusted to 1 mg ml^{-1} for flash freezing in
358 liquid nitrogen and storage at -80°C.

359 For the pulldown assay, 132 µg of 3C protease cleaved ABCA7 was mixed with pure his tagged
360 apoA1 using a 1:10 molar ratio in a buffer comprising 25 mM Hepes pH 7.5, 150 mM NaCl,

361 0.02%/0.004 % w:v DDM/CHS and incubated for 2 hours at 4°C with gentle agitation. The mixture
362 was then applied to 100 µl Ni-NTA beads equilibrated with wash buffer, and the binding was
363 allowed to proceed for 2 hours at 4°C with gentle agitation. The beads were washed with 4 x 10
364 BVs of wash buffer to remove unbound proteins. Bound proteins were eluted with 2 BVs elution
365 buffer (25 mM Hepes pH 7.5, 150 mM NaCl, 0.02%/0.004 % w:v DDM/CHS, 250 mM
366 Imidazole). The eluate was concentrated to 100 µl and the fractions run on sodium dodecyl sulfate
367 (SDS)–polyacrylamide gel electrophoresis (SDS–PAGE).

368 **ABCA7 Nanodisc and proteoliposome preparation**

369 For nanodisc reconstitution, peptide eluted or 3C cleaved ABCA7 was mixed with membrane
370 scaffold protein D1 (MSP1D1, addgene) and a mixture of BPL (Avanti polar lipids) and
371 cholesterol (80:20 w:w) containing 0.5%/0.1% DDM:CHS using a 1:10:350
372 (ABCA7:MSPD1:lipid mix) molar ratio, in nanodisc buffer (150 mM NaCl, 25 mM Hepes pH
373 7.5) containing up to 4% glycerol for 30 minutes at room temperature (RT). Nanodisc
374 reconstitution was induced by removing detergent with 0.8 $mg^{-1}ml^{-1}$ pre-washed Biobeads SM-2
375 (Bio-rad) for 2 hours with gentle agitation at RT. For different phospholipid compositions, BPL
376 was replaced with brain PE, brain PS, or Brain PS (all from Avanti polar lipids). For structural
377 studies, peptide eluted ABCA7 still bearing the eYFP-Rho1D4 tag was bound to rho-1D4 resin for
378 an additional 2 hours, washed with 4 BV of nanodisc buffer, and eluted with 3C protease for 2
379 hours at 4°C. The eluted ABCA7 nanodiscs were concentrated using a 100,000 MWCO kDa
380 Amicon filter and further purified by size exclusion chromatography using a G4000swxl column
381 (TOSOH biosciences) equilibrated with nanodisc buffer at 4°C (Figure S1A).

382 ABCA7 proteoliposomes were generated by mixing detergent purified ABCA7 with a 4:1 mixture
383 of BPL/cholesterol at a protein:lipid ratio of 1:10 w:w using the described protocol (Geertsma et

384 al., 2008). Proteoliposomes were resuspended at a final concentration of 0.5 - 1 mg ml^{-1}, aliquoted,
385 and flash frozen in liquid nitrogen for storage at -80°C.

386 **ATPase assays**

387 ATPase assays were based on a molybdate based colorimetric assay (Chifflet et al., 1988). Protein
388 concentrations used were in the range of 0.05-0.2 mg ml^{-1}. Assays were started by the addition of
389 2 mM ATP in the presence of 10 mM magnesium chloride ($MgCl_2$), incubated for 30 minutes at
390 37°C, then stopped by addition of 6% SDS. The assay was also performed in the presence of
391 ABCA7 inhibitors as additives, such as 5 mM ATPγS or sodium orthovanadate. For ATP K_M
392 measurements, a range of ATP concentrations was used. Linear regression analyses were carried
393 out using GraphPad Prism. All commercial apolipoproteins were purchased from Abcam,
394 resuspended as per manufacturer specifications and desalted into nanodisc buffer. 6,7-Dimethoxy-
395 2,4-quinazolinediamine (CAS 60547-96-8) was purchased from Toronto Research Chemicals and
396 resuspended in 100% DMSO. All reaction components were mixed with ABCA7 in detergent or
397 reconstituted in nanodiscs in the absence of ATP, incubated for 10 minutes at 37 °C prior to
398 addition of ATP to start the reaction.

399 **Cryo-electron microscopy grid preparation**

400 SEC purified nanodisc reconstituted ABCA7 was mixed with 5 mM ATPγS (Sigma) and 5 mM
401 $MgCl_2$ for 20 minutes at room temperature and concentrated to 0.2-0.5 mg ml^{-1}. 4 ul samples were
402 applied to glow discharged Quantifoil R1.2/1.3 grids (Electron Microscopy Sciences, Hatfield,
403 PA, USA) using a Vitrobot Mark IV (Thermo Fisher Scientific) with a 4s blotting time and 0
404 blotting force under >90% humidity at 4°C, then plunge frozen in liquid ethane.

405 **Cryo-electron microscopy data collection and processing.**

406 Grids were clipped as per manufacturer guidelines and cryo-EM data was collected using a Titan
407 Krios electron microscope operating at 300kV and equipped with a Falcon 3EC direct electron
408 detector (Thermo Fisher Scientific.). Automated data collection was carried out using EPU
409 (Thermo Fisher Scientific) over multiple sessions in counting mode at a nominal magnification of
410 96,000x, corresponding to a calibrated pixel size of 0.895 Å. Image stacks comprising 60 frames
411 were collected at a defocus range of -0.6 to -2.6 µm and estimated dose rate of 1 electron/ $Å^2$/frame
412 and further processed in Relion-3.1 (beta). Motion correction was done using Motioncor2 (Relion
413 implementation)(Zheng et al., 2017) and contrast transfer function (CTF) correction was
414 performed using Gctf (Zhang, 2016). A summary of the overall data processing scheme is
415 presented in Supplementary Figure S1C-E. In brief, 11802 micrographs were used for template
416 free picking of 6725108 particles, followed by particle extraction at a 3x binned pixel size of 2.685
417 Å/pix. The dataset was processed in two batches. After 2-3 rounds of 2D classification 1259324
418 particles from Set 1 and 1088487 particles from Set 2 were selected for independent 3D
419 classification steps (number of classes (K)=8 for both). The structure of human ABCA1
420 (EMDB6724) was used as a 3D reference for an initial 3D classification of a subset of the total
421 data to yield an initial sub-nanometer resolution map of ABCA7 that was used as a 3D reference
422 for the full datasets. After 1 round of 3D classification, both sets of data yielded a similar ensemble
423 of classes. A total of 113291 particles from similar looking classes (black boxes) were subjected
424 to an additional round of classification (K=3), ~80% of which fell into a high-resolution class that
425 yielded a 3.6 Å map after refinement and particle polishing steps. Similarly, 124114 particles from
426 a second set of two similar classes (red boxes in Figure S1D) were selected for subsequent
427 refinement, particle polishing, and post processing to yield a 3.2 Å map. All resolution estimates
428 were based on the gold standard 0.143 cutoff criterion (Scheres and Chen, 2012).

429 **Model building and refinement**

430 Model building was done in coot (Emsley et al., 2010) using a combination of Map 1 and its local
431 resolution filtered variant and Map 2. Both Map 1 and Map 2 displayed significant conformational
432 heterogeneity in the second half of ABCA7, with the quality of density in Map 1 allowing
433 placement of a TMD2 model guided in part by the homologous ABCA1 structure. Density
434 attributed to inter-TMD phospholipids was clearest in Map 1. Map 2 revealed very poor and
435 discontinuous density for TMD2-NBD2 but significantly better density for TMD1-NBD1 and the
436 majority of ECD1 and ECD2, allowing for *de novo* model building. The model for ECD was also
437 guided by the presence of nine glycosylation sites (N78, N98, N312, N340, N1335, N1381, N1386,
438 N1457, & N1518) as well as 4 disulfide bond pairs. Density for the lid region of the ECD was
439 missing in both maps. Model building for both NBDs was guided by structures of the homologous
440 transporters TM287 (Hohl et al., 2012), ABCG2, and ABCA1, where density features did not allow
441 for *de novo* model building. We observed extra density at the nucleotide binding sites for both
442 NBDs despite their open conformation. The structure of the RD was based on a homology model
443 of the predicted RD structure in ABCA1. The quality of density for the ABCA7 RD allowed rigid
444 body placement for the entire domain. Restrained real space refinement of the model was carried
445 out in Phenix (Adams et al., 2010) using automatically generated secondary structure restraints.
446 Structure figures were prepared in UCSF Chimera (Pettersen et al., 2004) and Pymol (The PyMOL
447 Molecular Graphics System, Version 1.8 Schrödinger, LLC).

448 **Acknowledgments**

449 We would like to thank Dr. Kaspar Locher at ETH, Zurich, Switzerland, for providing the synthetic
450 gene construct of ABCA7. We would also like to thank the cryo-EM and shared instruments core
451 facilities at the Hormel Institute for help with experimental setup and Dr. Rhoderick Brown, Dr.

452 Jarrod French, and Dr. Jeppe Olsen for critical reading and discussion during manuscript
453 preparation. This work was supported in part by the Hormel Foundation (Institutional research
454 funds to AA), the EAGLES Cancer Telethon Postdoctoral Fellowship (to LTML) and the Cure
455 Alzheimer's fund (to TK).

456 **Author Contributions**

457 AA conceived the research. LTML, JRT, and AA performed all research. TA and TK provided
458 information on DADMQ and participated in assay design. LTML, JRT, and AA wrote the
459 manuscript with input from all other authors.

460 **Declaration of Interests**

461 The authors declare no competing interests.

462 **Data and materials availability:**

463 The cryo-EM Maps for nanodisc reconstituted human ABCA7 have been deposited at the Elecron
464 Microscopy Databank (EMDB) under accession codes EMD-22996 and EMD-22998 for Map 1
465 and Map 2, respectively. The associated atomic coordinates have been deposited at the Protein
466 Data bank (PDB) under accession code 7KQC.

467 **References**

468 Abe-Dohmae, S.Y., S. (2012). ABCA7: a potential mediator between cholesterol homeostasis
469 and the host defense system. Clinical Lipidology *7*, 677-687.

470 Adams, P.D., Afonine, P.V., Bunkoczi, G., Chen, V.B., Davis, I.W., Echols, N., Headd, J.J.,
471 Hung, L.W., Kapral, G.J., Grosse-Kunstleve, R.W.*, et al.* (2010). PHENIX: a comprehensive
472 Python-based system for macromolecular structure solution. Acta Crystallogr D Biol Crystallogr
473 *66*, 213-221.

474 Alam, A., Kung, R., Kowal, J., McLeod, R.A., Tremp, N., Broude, E.V., Roninson, I.B.,
475 Stahlberg, H., and Locher, K.P. (2018). Structure of a zosuquidar and UIC2-bound human-
476 mouse chimeric ABCB1. Proc Natl Acad Sci U S A *115*, E1973-E1982.
477 Almeida, J.F.F., Dos Santos, L.R., Trancozo, M., and de Paula, F. (2018). Updated Meta-
478 Analysis of BIN1, CR1, MS4A6A, CLU, and ABCA7 Variants in Alzheimer's Disease. J Mol
479 Neurosci *64*, 471-477.
480 Association, A.s. (2020). 2020 Alzheimer's disease facts and figures. Alzheimers Dement.
481 Bellenguez, C., Charbonnier, C., Grenier-Boley, B., Quenez, O., Le Guennec, K., Nicolas, G.,
482 Chauhan, G., Wallon, D., Rousseau, S., Richard, A.C.*, et al.* (2017). Contribution to Alzheimer's
483 disease risk of rare variants in TREM2, SORL1, and ABCA7 in 1779 cases and 1273 controls.
484 Neurobiol Aging *59*, 220 e221-220 e229.
485 Chifflet, S., Torriglia, A., Chiesa, R., and Tolosa, S. (1988). A method for the determination of
486 inorganic phosphate in the presence of labile organic phosphate and high concentrations of
487 protein: application to lens ATPases. Anal Biochem *168*, 1-4.
488 De Roeck, A., Van Broeckhoven, C., and Sleegers, K. (2019). The role of ABCA7 in
489 Alzheimer's disease: evidence from genomics, transcriptomics and methylomics. Acta
490 Neuropathol *138*, 201-220.
491 Emsley, P., Lohkamp, B., Scott, W.G., and Cowtan, K. (2010). Features and development of
492 Coot. Acta Crystallogr D Biol Crystallogr *66*, 486-501.
493 Fitzgerald, M.L., Morris, A.L., Rhee, J.S., Andersson, L.P., Mendez, A.J., and Freeman, M.W.
494 (2002). Naturally occurring mutations in the largest extracellular loops of ABCA1 can disrupt its
495 direct interaction with apolipoprotein A-I. J Biol Chem *277*, 33178-33187.

496 Fitzgerald, M.L., Okuhira, K., Short, G.F., 3rd, Manning, J.J., Bell, S.A., and Freeman, M.W.
497 (2004). ATP-binding cassette transporter A1 contains a novel C-terminal VFVNFA motif that is
498 required for its cholesterol efflux and ApoA-I binding activities. J Biol Chem *279*, 48477-48485.
499 Geertsma, E.R., Nik Mahmood, N.A., Schuurman-Wolters, G.K., and Poolman, B. (2008).
500 Membrane reconstitution of ABC transporters and assays of translocator function. Nat Protoc *3*,
501 256-266.
502 Hohl, M., Briand, C., Grutter, M.G., and Seeger, M.A. (2012). Crystal structure of a
503 heterodimeric ABC transporter in its inward-facing conformation. Nat Struct Mol Biol *19*, 395-
504 402.
505 Hollingworth, P., Harold, D., Sims, R., Gerrish, A., Lambert, J.C., Carrasquillo, M.M., Abraham,
506 R., Hamshere, M.L., Pahwa, J.S., Moskvina, V.*, et al.* (2011). Common variants at ABCA7,
507 MS4A6A/MS4A4E, EPHA1, CD33 and CD2AP are associated with Alzheimer's disease. Nat
508 Genet *43*, 429-435.
509 Ikeda, Y., Abe-Dohmae, S., Munehira, Y., Aoki, R., Kawamoto, S., Furuya, A., Shitara, K.,
510 Amachi, T., Kioka, N., Matsuo, M.*, et al.* (2003). Posttranscriptional regulation of human
511 ABCA7 and its function for the apoA-I-dependent lipid release. Biochem Biophys Res Commun
512 *311*, 313-318.
513 Iwamoto, N., Abe-Dohmae, S., Sato, R., and Yokoyama, S. (2006). ABCA7 expression is
514 regulated by cellular cholesterol through the SREBP2 pathway and associated with phagocytosis.
515 J Lipid Res *47*, 1915-1927.
516 Lambert, J.C., Ibrahim-Verbaas, C.A., Harold, D., Naj, A.C., Sims, R., Bellenguez, C.,
517 DeStafano, A.L., Bis, J.C., Beecham, G.W., Grenier-Boley, B.*, et al.* (2013). Meta-analysis of

518 74,046 individuals identifies 11 new susceptibility loci for Alzheimer's disease. Nat Genet *45*,
519 1452-1458.
520 Le Guennec, K., Nicolas, G., Quenez, O., Charbonnier, C., Wallon, D., Bellenguez, C., Grenier-
521 Boley, B., Rousseau, S., Richard, A.C., Rovelet-Lecrux, A.*, et al.* (2016). ABCA7 rare variants
522 and Alzheimer disease risk. Neurology *86*, 2134-2137.
523 Lee, J.Y., Kinch, L.N., Borek, D.M., Wang, J., Wang, J., Urbatsch, I.L., Xie, X.S., Grishin, N.V.,
524 Cohen, J.C., Otwinowski, Z.*, et al.* (2016). Crystal structure of the human sterol transporter
525 ABCG5/ABCG8. Nature *533*, 561-564.
526 Lee, J.Y., Yang, J.G., Zhitnitsky, D., Lewinson, O., and Rees, D.C. (2014). Structural basis for
527 heavy metal detoxification by an Atm1-type ABC exporter. Science *343*, 1133-1136.
528 Liu, F., Lee, J., and Chen, J. (2021). Molecular structures of the eukaryotic retinal importer
529 ABCA4. Elife *10*.
530 Ma, F.C., Wang, H.F., Cao, X.P., Tan, C.C., Tan, L., and Yu, J.T. (2018). Meta-Analysis of the
531 Association between Variants in ABCA7 and Alzheimer's Disease. J Alzheimers Dis *63*, 1261-
532 1267.
533 Manolaridis, I., Jackson, S.M., Taylor, N.M.I., Kowal, J., Stahlberg, H., and Locher, K.P. (2018).
534 Cryo-EM structures of a human ABCG2 mutant trapped in ATP-bound and substrate-bound
535 states. Nature *563*, 426-430.
536 Meurs, I., Calpe-Berdiel, L., Habets, K.L., Zhao, Y., Korporaal, S.J., Mommaas, A.M., Josselin,
537 E., Hildebrand, R.B., Ye, D., Out, R.*, et al.* (2012). Effects of deletion of macrophage ABCA7
538 on lipid metabolism and the development of atherosclerosis in the presence and absence of
539 ABCA1. PLoS One *7*, e30984.

540 Molday, L.L., and Molday, R.S. (2014). 1D4: a versatile epitope tag for the purification and
541 characterization of expressed membrane and soluble proteins. Methods Mol Biol *1177*, 1-15.
542 Nagao, K., Takahashi, K., Azuma, Y., Takada, M., Kimura, Y., Matsuo, M., Kioka, N., and
543 Ueda, K. (2012). ATP hydrolysis-dependent conformational changes in the extracellular domain
544 of ABCA1 are associated with apoA-I binding. J Lipid Res *53*, 126-136.
545 Nosol, K., Romane, K., Irobalieva, R.N., Alam, A., Kowal, J., Fujita, N., and Locher, K.P.
546 (2020). Cryo-EM structures reveal distinct mechanisms of inhibition of the human multidrug
547 transporter ABCB1. Proc Natl Acad Sci U S A *117*, 26245-26253.
548 Olsen, J.A., Alam, A., Kowal, J., Stieger, B., and Locher, K.P. (2020). Structure of the human
549 lipid exporter ABCB4 in a lipid environment. Nat Struct Mol Biol *27*, 62-70.
550 Orlando, B.J., and Liao, M. (2020). ABCG2 transports anticancer drugs via a closed-to-open
551 switch. Nat Commun *11*, 2264.
552 Pettersen, E.F., Goddard, T.D., Huang, C.C., Couch, G.S., Greenblatt, D.M., Meng, E.C., and
553 Ferrin, T.E. (2004). UCSF Chimera--a visualization system for exploratory research and
554 analysis. J Comput Chem *25*, 1605-1612.
555 Qian, H., Zhao, X., Cao, P., Lei, J., Yan, N., and Gong, X. (2017). Structure of the Human Lipid
556 Exporter ABCA1. Cell *169*, 1228-1239 e1210.
557 Quazi, F., and Molday, R.S. (2013). Differential phospholipid substrates and directional transport
558 by ATP-binding cassette proteins ABCA1, ABCA7, and ABCA4 and disease-causing mutants. J
559 Biol Chem *288*, 34414-34426.
560 Scheres, S.H., and Chen, S. (2012). Prevention of overfitting in cryo-EM structure determination.
561 Nat Methods *9*, 853-854.

562 Sleegers, K. (2020). Expression of ABCA7 in Alzheimer's disease. Acta Neuropathol *139*, 941-
563 942.
564 Swerdlow, R.H. (2016). Rare ABCA7 variants in Alzheimer disease: Guilt by association.
565 Neurology *86*, 2118-2119.
566 Tanaka, N., Abe-Dohmae, S., Iwamoto, N., Fitzgerald, M.L., and Yokoyama, S. (2010). Helical
567 apolipoproteins of high-density lipoprotein enhance phagocytosis by stabilizing ATP-binding
568 cassette transporter A7. J Lipid Res *51*, 2591-2599.
569 Thomas, C., Aller, S.G., Beis, K., Carpenter, E.P., Chang, G., Chen, L., Dassa, E., Dean, M.,
570 Duong Van Hoa, F., Ekiert, D.*, et al.* (2020). Structural and functional diversity calls for a new
571 classification of ABC transporters. FEBS Lett *594*, 3767-3775.
572 Tomioka, M., Toda, Y., Manucat, N.B., Akatsu, H., Fukumoto, M., Kono, N., Arai, H., Kioka,
573 N., and Ueda, K. (2017). Lysophosphatidylcholine export by human ABCA7. Biochim Biophys
574 Acta Mol Cell Biol Lipids *1862*, 658-665.
575 Voloshyna, I., and Reiss, A.B. (2011). The ABC transporters in lipid flux and atherosclerosis.
576 Prog Lipid Res *50*, 213-224.
577 Wang, N., Lan, D., Gerbod-Giannone, M., Linsel-Nitschke, P., Jehle, A.W., Chen, W., Martinez,
578 L.O., and Tall, A.R. (2003). ATP-binding cassette transporter A7 (ABCA7) binds apolipoprotein
579 A-I and mediates cellular phospholipid but not cholesterol efflux. J Biol Chem *278*, 42906-
580 42912.
581 Wu, Y.C., and Horvitz, H.R. (1998). The C. elegans cell corpse engulfment gene ced-7 encodes a
582 protein similar to ABC transporters. Cell *93*, 951-960.
583 Zhang, K. (2016). Gctf: Real-time CTF determination and correction. J Struct Biol *193*, 1-12.

584 Zheng, S.Q., Palovcak, E., Armache, J.P., Verba, K.A., Cheng, Y., and Agard, D.A. (2017).
585 MotionCor2: anisotropic correction of beam-induced motion for improved cryo-electron
586 microscopy. Nat Methods *14*, 331-332.
587
588
589
590
591
592
593
594
595
596
597
598
599
600
601
602
603
604
605
606

607 **Figures and Legends**

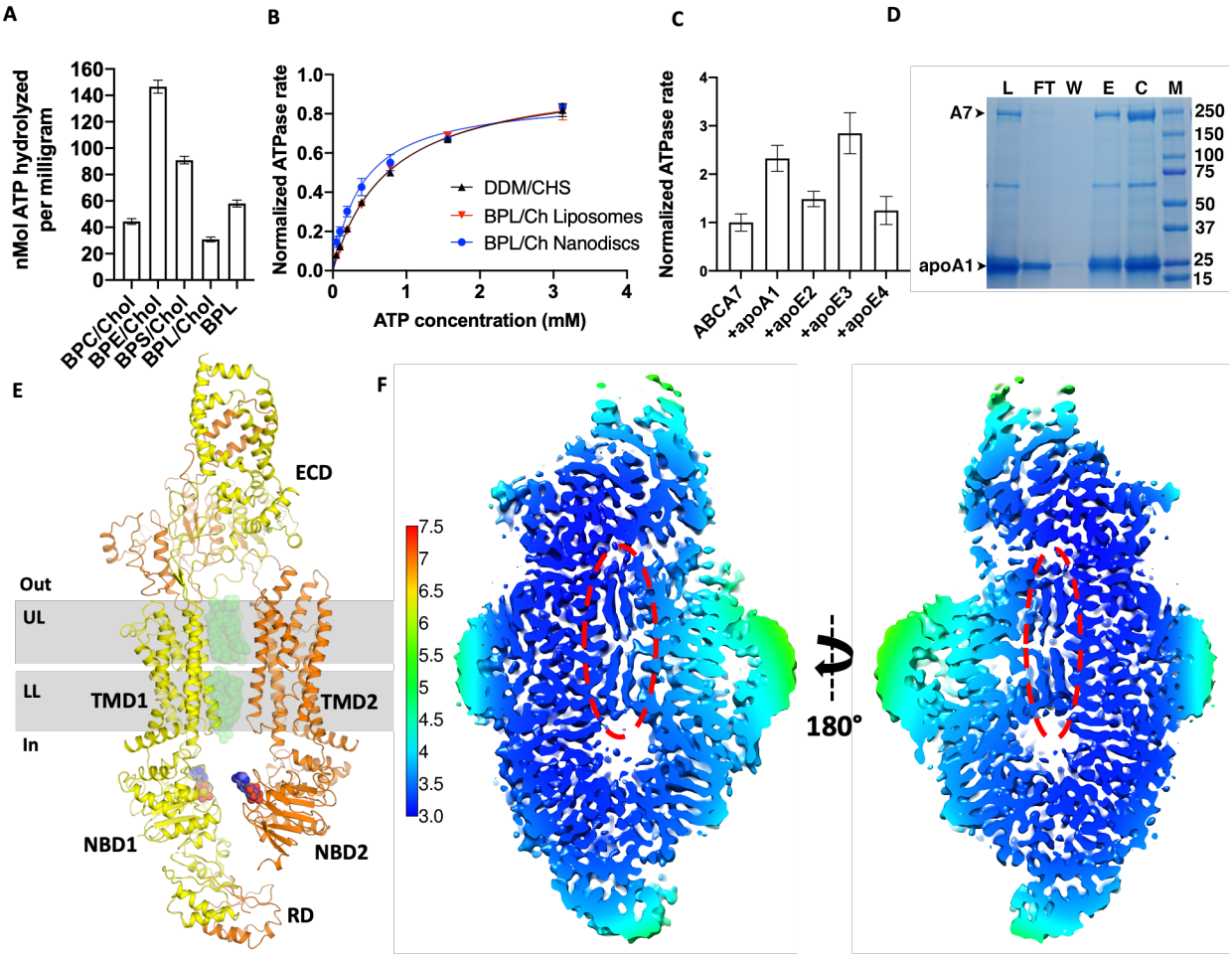

608

609 **Figure 1. Overall structural and functional characterization of human ABCA7 (A)** ABCA7
610 ATPase activity in nanodiscs of different phospholipid/cholesterol compositions. **(B)** ATPase.
611 Activity of ABCA7 at different ATP concentrations. (**C**) ABCA7 ATPase rates in the presence of
612 apoA1 and apoE1-4. **(D)** SDS-PAGE gel of ABCA7-apoA1 pulldown. L= ABCA7 + apoA1 Load.
613 FT= flowthrough, W=final wash, E = eluate, C= concentrated eluate, M= molecular weight
614 marker. **(E)** Overall structure of nanodisc reconstituted ABCA7. The two halves are shown as
615 yellow and orange ribbons, respectively. Bound nucleotides are shown as solid spheres. Grey bars
616 represent the membrane upper leaflet (UL) and lower leaflet (LL) and modeled lipids as transparent

617 green spheres. (**F**) Local resolution filtered cryo-EM map of human ABCA7. Dashed red ovals
618 demarcate location of TMD lipids. ATPase data reported are for three independent experimental
619 replicates (n=3) and error bars represent standard.
620
621
622
623
624
625
626
627
628

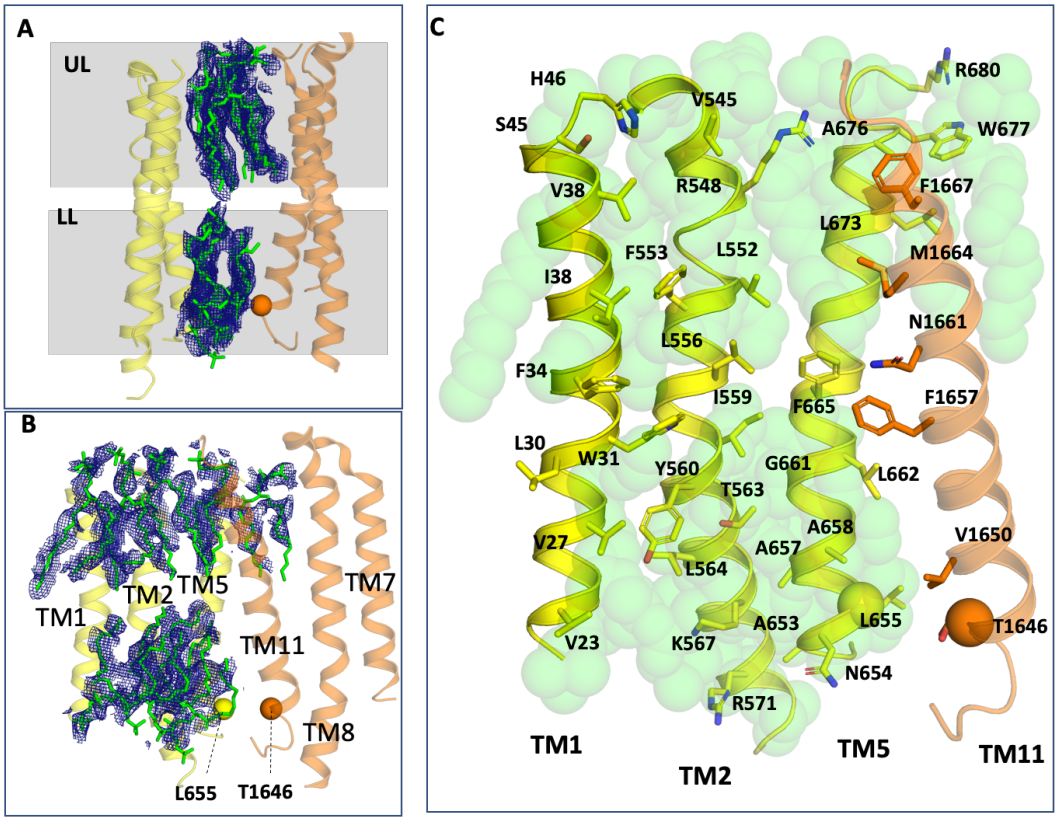

Fig. 2. Details of TMD and lipid filled transmembrane pathway (A) Central lipid filled transmembrane cavity with cavity lining TMs shown as ribbons. Intracellular gate forming residues L655 and T1646 are shown as yellow and orange spheres, respectively. Green sticks indicate lipids and EM density is shown as blue mesh contoured at 6σ. **(B)** same as panel A viewed from side **(C)** Detailed view from panel B with sidechains from residues within 5Å of observed TMD lipids shown as sticks and labeled. Lipids are represented as transparent green spheres.

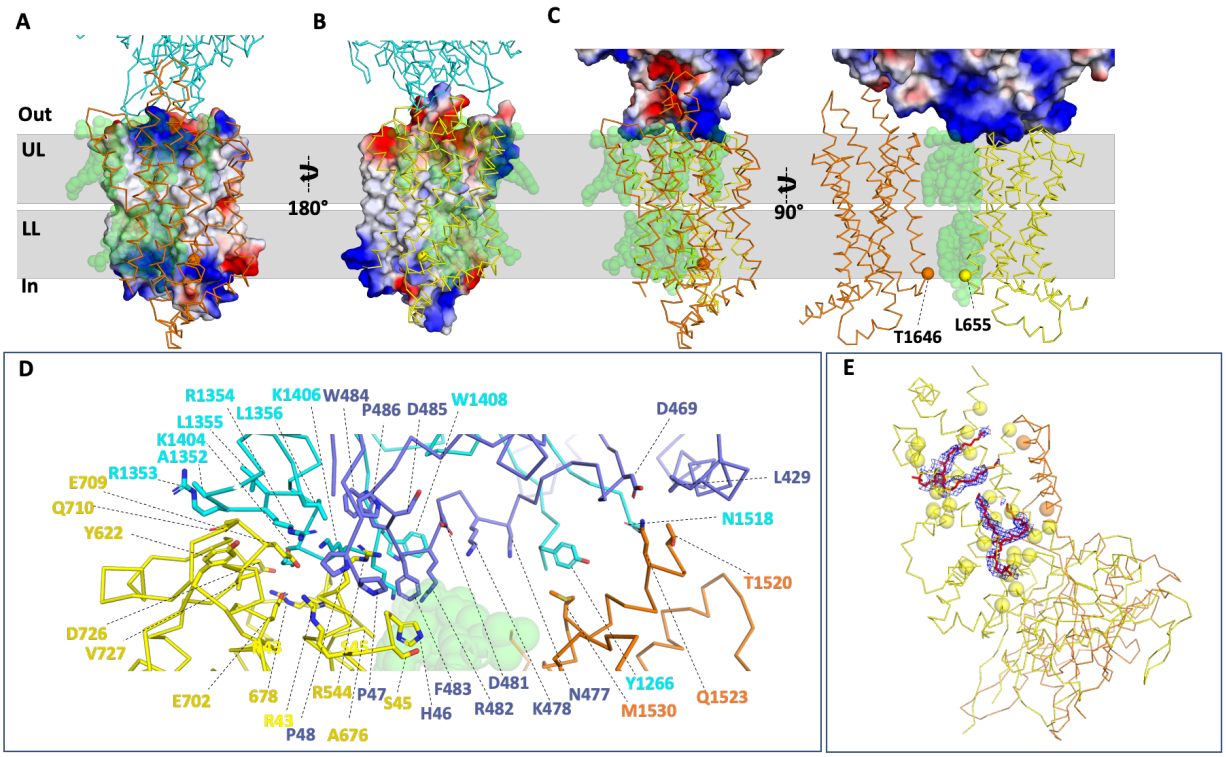

Fig. 3. Details of ECD-TMD and lipid facing interfaces. Electrostatic potential maps focusing on **(A)** TMD1, **(B)** TMD2, and **(C)** the ECD. Lipids are shown as transparent green spheres, TMD1 in yellow (B-C), TMD2 in orange ribbon (A, C) the ECD in cyan (A, B) colored ribbons. **D** TMD-ECD binding interface with TMD1 and TMD2 colored yellow an orange respectively, and ECD1 and ECD 2 colored purple and cyan, respectively. TMD1 and TMD2 residues within 4Å of either ECD are labeled yellow and orange, respectively. ECD1 and ECD2 residues within within 4Å of either TMD are labeled purple and cyan, respectively. **(E)** Unspecified ECD lipids (magenta sticks) and their corresponding EM density (blue mesh) within the ECD hydrophobic tunnel. TMD 1 and TMD 2 are colored yellow and orange respectively, molecules are shown as green sticks. Cα atoms for residues within 5Å of observed lipids are shown as spheres.

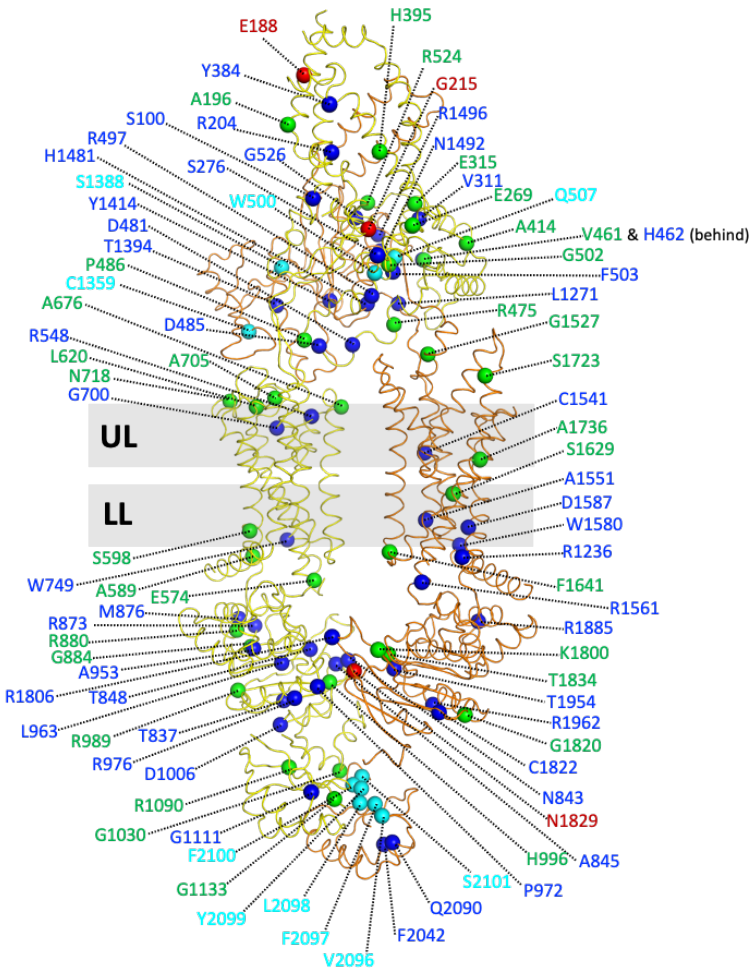

649

650 **Figure 4 Known amino acid variants of ABCA7.** Structure of ABCA7 with Cα atoms shown
651 for pathogenic variants (green), protective variants (red), and residues conserved in ABCA1 and
652 ABCA7 known to disrupt the latter's binding to apoA1 and/or phospholipid translocation (blue).
653 Cyan spheres highlight residue positions of ABCA1 mutations known to disrupt phospholipid
654 efflux including those equivalent to the VFVNFA motif within the ABCA1 RD. Grey bars indicate
655 the upper and lower membrane bilayer leaflets (UL and LL, respectively).

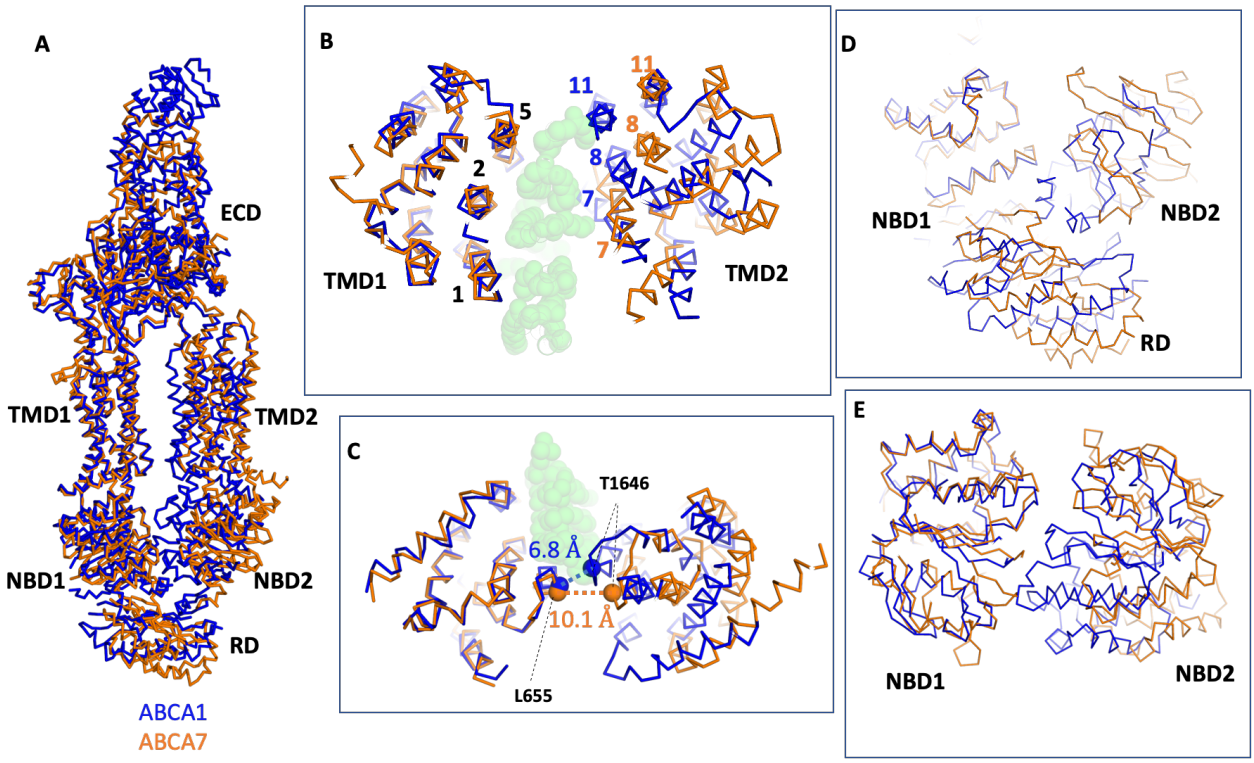

656

657 **Figure 5. Conservation of ABCA7 and ABCA1 structural elements (A)** Ribbon representation
658 of select ABCG family transporter structures with rcsb codes. Overall structural alignment of
659 ABCA7 (blue) and ABCA1 (rose). (**B**) Alignment of TMD1 and TMD2 of ABCA1 and ABCA7
660 with individual TMs labeled, viewed from the extracellular side. (**C**) Same as panel B, viewed
661 from the cytoplasmic side. **(D)** Front view of NBD1, NBD2, and the RD of ABCA7 aligned to
662 those of ABCA. **(E)** ABCA7-ABCA1 NBD alignment viewed from the extracellular side with the
663 ECD and TMDs removed for clarity.

664

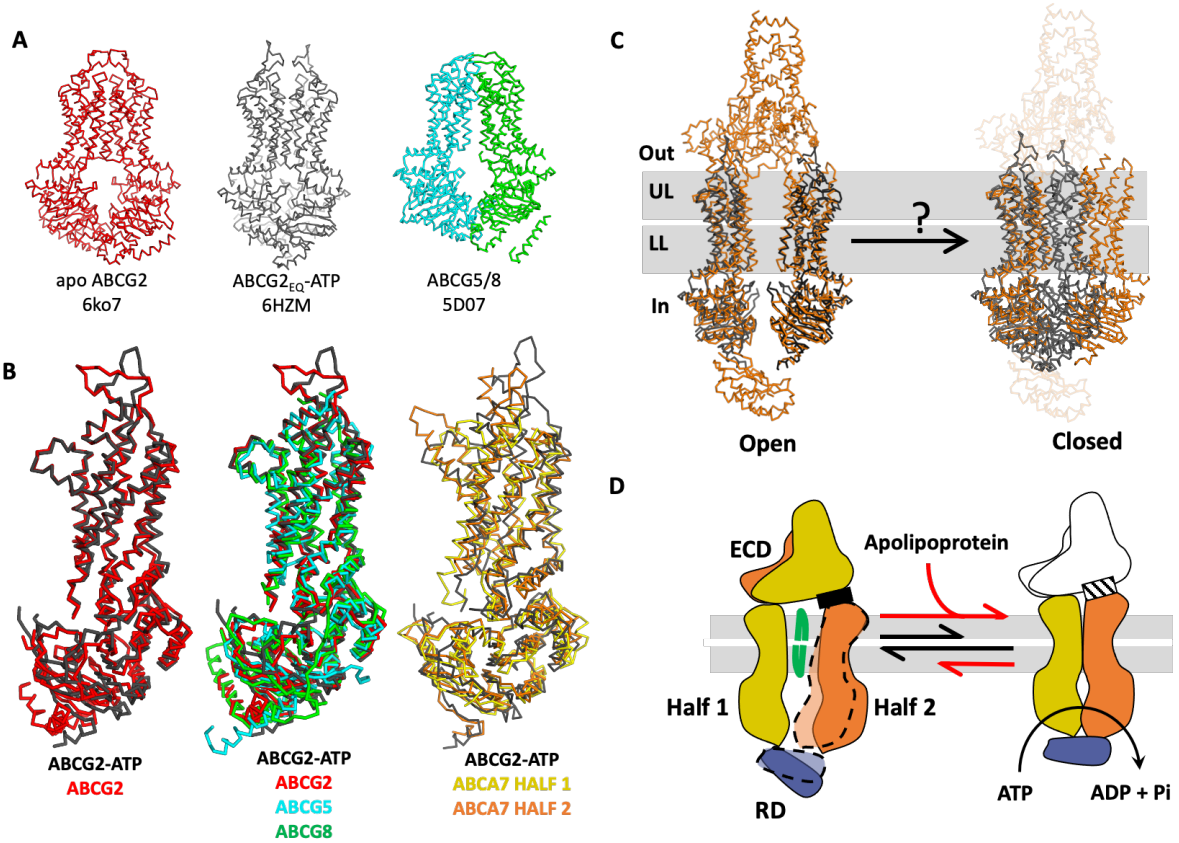

665

666 **Figure 6. Conservation of ABCA and ABCG family structural elements (A)** Ribbon
667 representation of select ABCG family transporter structures and their respective PDB IDs
668 including apo open ABCG2 (black), closed ATP bound structure of $ABCG2_{EQ}$ (black), and
669 ABCG5/G8 (cyan and green, respectively) (**B**) Alignment of NBD-TMD pairs from open and
670 closed conformations of ABCG2 (left), ABCG2 and ABCG5/G8 (center), and closed ABCG2 with
671 TMD-NBD pairs from ABCA7 half 1 (gold) and half 2 (orange). **(C)** Alignment of both ABCA7
672 TMD-NBD pairs with NBD-TMD pair from closed $ABCG2_{EQ}$-ATP (left) and superposition of the
673 full $ABCG2_{EQ}$-ATP structure onto ABCA7 aligned with respect to TMD1-NBD1. Arrow and
674 question mark indicate proposed transition from the former, open state to the latter hypothetical
675 closed state based on ABCG2 with ECD and ED shown as transparent ribbons. (**D**) Hypothetical

676 model of apolipoprotein induced structural transitions in ABCA7. The ECD TMD interface is
677 shown as solid black rectangle or dashed rectangle. Phospholipids are shown as green lines.
678
679
680
681
682
683
684
685
686
687
688
689
690
691
692
693

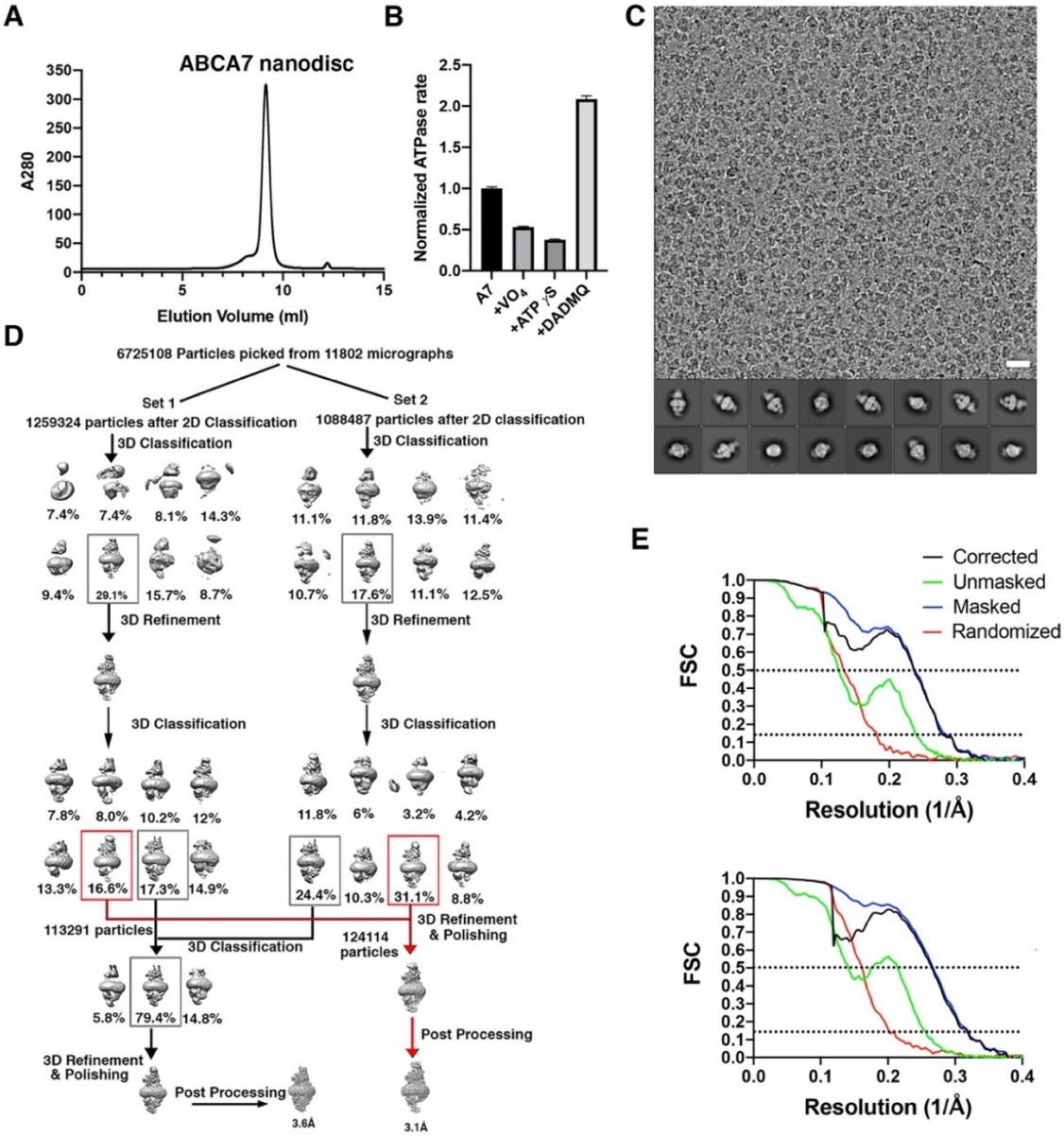

Figure S1. Cryo-EM data processing workflow for nanodisc reconstituted ABCA7 (A) Size exclusion chromatography micrograph of cryo-EM sample showing monodisperse ABCA7 nanodisc (main peak). (**B)** ATPase data nanodisc reconstituted ABCA7 in the presence of sodium orthovanadate ($V0_4$), ATPγS, and DADMQ normalized to apo ABCA7 ATPase rate. N=3 and error bars represent s.d. **C** Representative micrograph at -2.5 µm defocus. Scale bar = 20 nm. **D** EM processing workflow. Boxes indicate 3D classes used for further refinement for both Map 1 and

701 Map 2 (red). **E** Fourier shell correlation (FSC) curves for Map 1 (top) and Map 2 (bottom). Dotted

702 lines indicate position 0.143 and 0.5 cutoff criteria for resolution estimates.

703

704

705

706

707

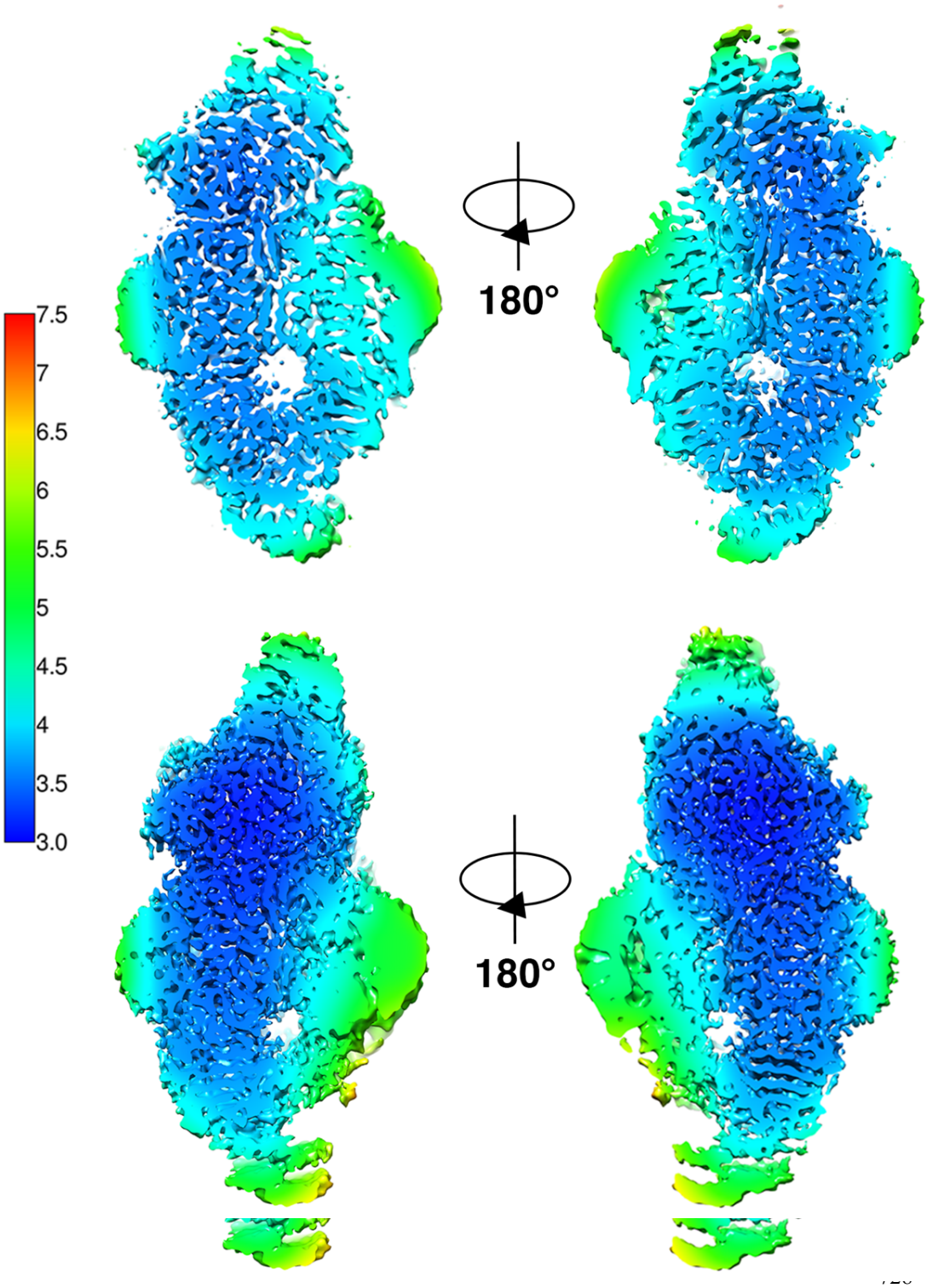

Figure S2. Local resolution-colored maps Central slices through Map 1 (top) and Map 2 (bottom) colored by local resolution.

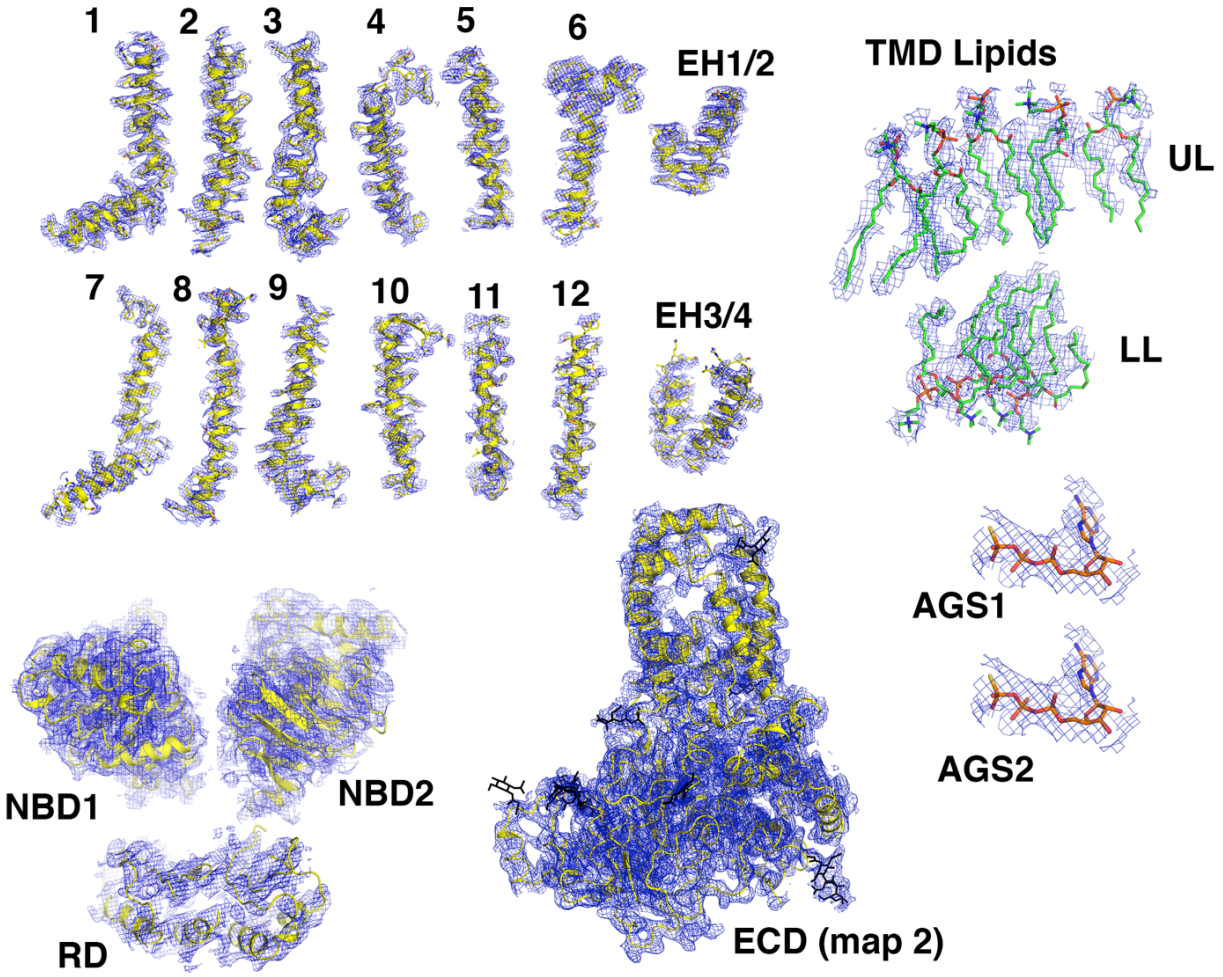

Figure S3. Quality of EM density for ABCA7 nanodisc TM helices are numbered. ECD density is shown for Map 2, all other density is for Map 1 contoured at 6σ. TMD phospholipids (modeled as phosphatidylcholine molecules) are shown as green sticks, Glycans as black sticks, andATP γS (AGS) molecules as red sticks. EH = external helix. UL and LL represent upper leaflet and lower leaflet lipids, respectively.

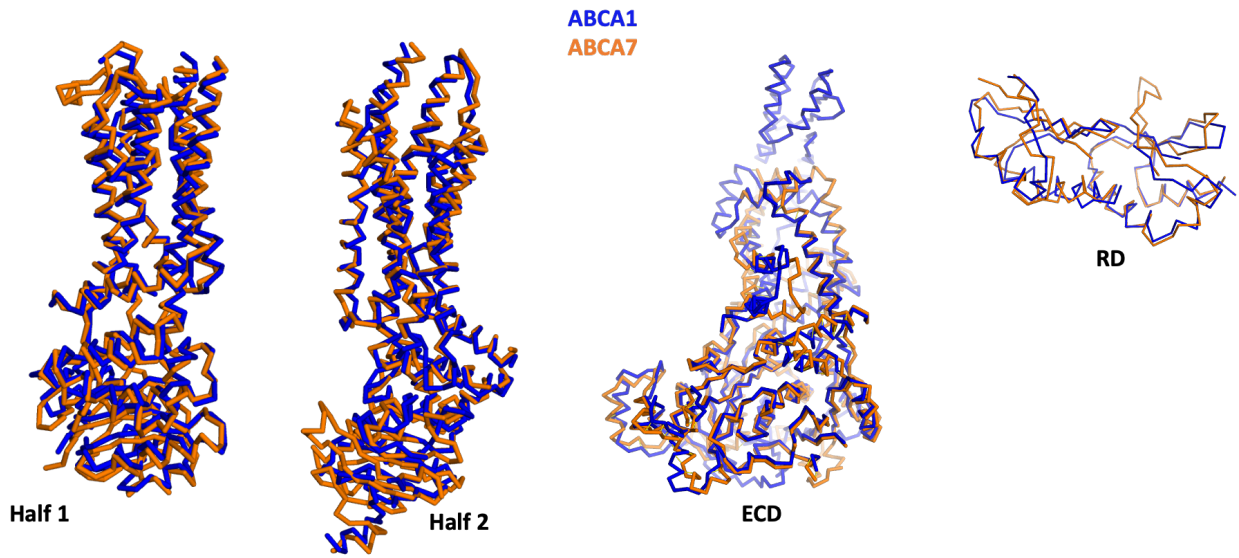

741

742 **Figure S4. ABCA7 and ABCA4 alignment** Superpositions of individual domains of nanodisc
743 reconstituted ABCA7 and detergent purified ABCA1. Individual TMD-NBD pairs were separately
744 aligned (Half 1 and Half 2 for TMD1-NBD1 and TMD2-NBD2, respectively) as were the ECD
745 and RD.

746

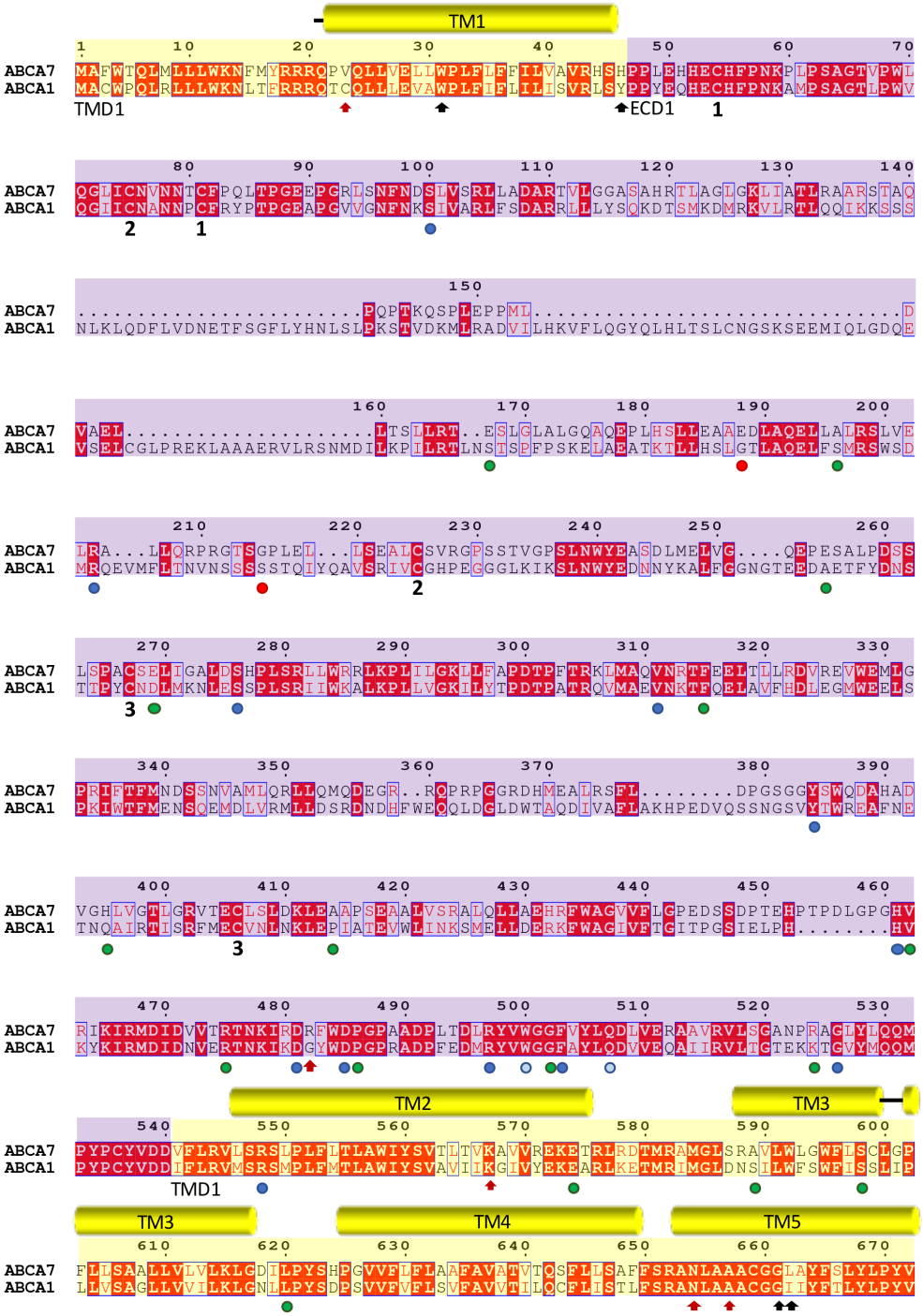

747

748

749

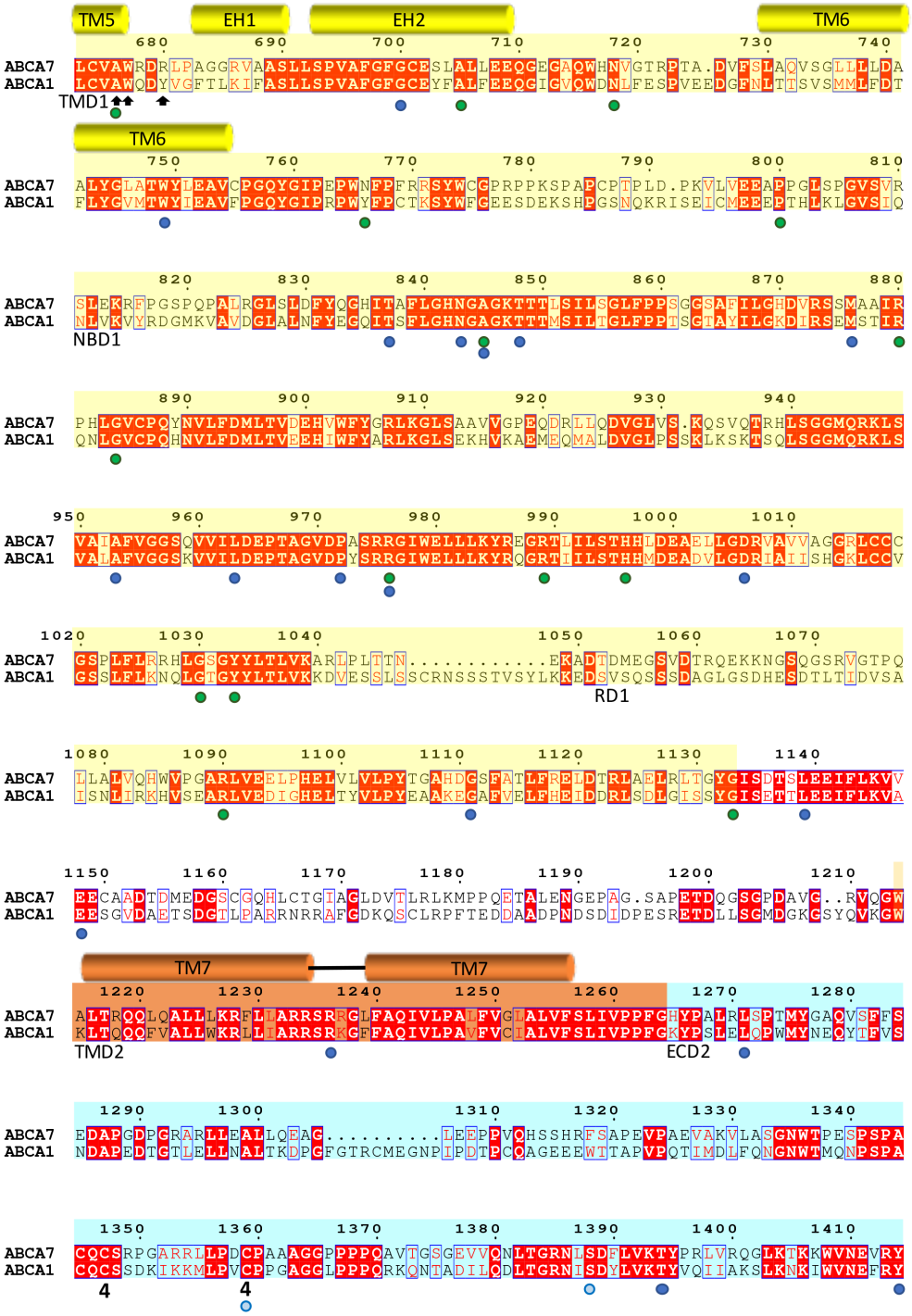
TM5
EH1
EH2
TM6
ABCA7
ABCA1
TMD1
TM6
NBD1
RD1
TM7
TM7
TMD2
ECD2

750

751

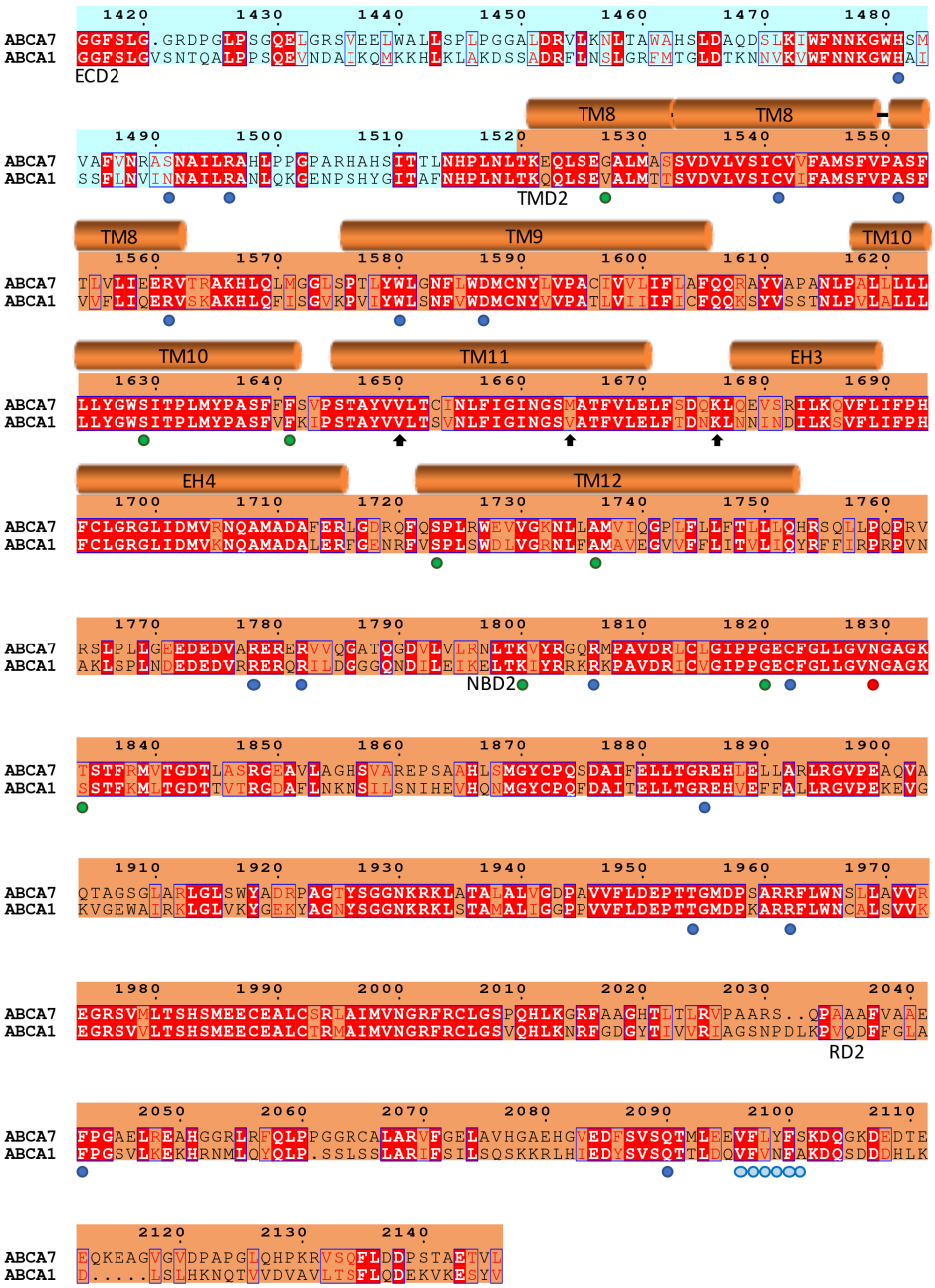

Figure S5 Sequence alignment of human ABCA7 and human ABCA1 Blue dots indicate residues known to be important for apoA1 binding in ABCA1. Numbers indicate disulfide bond pairs. Green and red dots inidicate residue positions of naturally occuring pathogenic or protective

757 variants in ABCA7, respectively. Cyan dots indicate residue positions in ABCA1 thought to
758 disrupt phospholipid efflux.
759
760
761
762
763
764
765
766
767
768
769
770
771
772
773
774
775
776
777
778
779

Dataset	Nanodisc reconstituted human ABCA7	
Magnification	96k	
Pixel Size (Å)	0.895	
Total Dose (e/Å^2)	60	
Defocus Range (um)	-0.8 to 2.6	
Maps	Map 1	Map 2
EMDB ID	EMD-22996	EMD-22998
# Particles in final Class	91381	124114
Resolution (Å) (0.143 threshold)	3.6	3.2
Sharpening B factor		
Refined Coordinates	Human ABCA7	
PDB ID	7KQC	
# Residues/Non-hydrogen Atoms/Ligands	1801/14611/28	
R.M.S deviations		
Bond Angles (Å)	0.006	
Bond lengths (°)	0.824	
MolProbity Statistics		
Molprobity Score	1.84	
Clashscore	8.84	
Poor rotamers (%)	0.41	
Ramachandran statistics		
Favored (%)	94.72	

Allowed (%)	4.83
Outliers (%)	0.45

780

781 **Table S1 Data collection and refinement statistics.**

782

783